

DEPARTURE AND TRAJECTORY DESIGN APPLICATIONS USING STRETCHING DIRECTIONS

Vivek Muralidharan* and Kathleen C. Howell†

Stable or nearly stable orbits do not always possess well-distinguished manifold structures that assist in departing from or arriving onto the orbit. Generally, for potential missions, the orbits of interest are nearly stable to reduce the possibility of rapid departure. The stable nature of these orbits also serves as a drawback for insertion or departure from the orbit. The Near Rectilinear Halo Orbits (NRHOs) and the Distant Retrograde Orbits (DROs) offer some potential long-horizon trajectories for exploration missions. The current investigation focuses on leveraging the stretching direction as a tool for departure and trajectory design applications. The magnitude of the state variations along the maximum stretching direction is expected to grow rapidly and, therefore, offers information for efficient departure from the orbit. Similarly, the maximum stretching in reverse time, enables arrival with a minimal maneuver magnitude.

INTRODUCTION

With the long term potential of NASA's Lunar Gateway facility, there is a growing interest in accessing nearby stable cislunar orbits for various mission scenarios. Near Rectilinear Halo Orbits (NRHOs) are members of the family of halo orbits in the L1 and L2 regions in the Earth-Moon system that offer potential candidates suitable for any long term presence. These NRHOs are stable or nearly stable as characterized by the linear variational flow in the circular restricted three-body problem (CR3BP).^{1,2} The near rectilinear halo orbits offer reasonably close lunar passages and large out-of-plane amplitudes relative to the Earth-Moon orbit plane, appropriate for investigating the polar regions of the Moon. Similar to the NRHOs, the Distant Retrograde Orbits (DROs) offer a range of stable orbits in the Earth-Moon system. The DROs are potential hosts for proposed propellant depots, that reduce costs to access various cislunar orbits and enable transfer options to interplanetary orbits.^{3,4} The Lunar Distant Retrograde Orbit (DRO), approximately 70,000 km from the Moon, served as the baseline for the previously investigated Asteroid Redirect Mission (ARM).⁵

With the increasing number of mission scenarios and with a potential human presence, an important capability is transfers between various locations of interest relatively quickly and cost efficiently. Disposal of logistic modules, for example, while avoiding any collisions is also a concern. Manifolds have been used extensively for orbit departure and trajectory design, however, the lack of well-distinguished stable and unstable manifold structures on orbits that are nearly stable is a challenge. Previous transfer trajectory design approaches linking stable orbits exploit intermediate segments of known orbits, resonant arcs as well as manifolds of known unstable orbits,⁶⁻¹⁰ however, the most productive types of intermediate orbits are not known *a priori*. In this investigation, the dynamical flow is visualized using the principal stretching directions. Variants from

*Ph.D. Candidate, School of Aeronautics and Astronautics, Purdue University, West Lafayette, IN 47907, USA, muralidv@purdue.edu; currently, Postdoctoral Researcher, Université du Luxembourg, L-1855 Luxembourg, vivek.muralidharan@uni.lu

†Hsu Lo Distinguished Professor of Aeronautics and Astronautics, School of Aeronautics and Astronautics, Purdue University, West Lafayette, IN 47907, USA, howell@purdue.edu

the stretching directions have been employed for multiple space applications, for example, stationkeeping,^{2,11-14} trajectory design (e.g., the EQUULEUS mission^{15,16}), sensitivity analysis along quasi-satellite orbits,¹⁷ patch-point placements along sensitive trajectories,¹⁸ as well as monitoring perturbation growth along trajectories.¹⁹ An alternate strategy that offers reliable departure and arrival analysis from stable orbits are explored in this investigation, one that leverages the maximum stretching directions. An effective departure from the orbit serves as a preliminary step for the disposal problem as well as a basis for transfers to other spatial locations.

CIRCULAR RESTRICTED THREE-BODY PROBLEM (CR3BP)

The circular restricted three-body problem (CR3BP) is a time invariant approximation for the spacecraft dynamics in the higher-fidelity ephemeris model. The CR3BP model characterizes the motion of a spacecraft influenced by the gravitational forces of two primary bodies, e.g., the Earth and the Moon, each rotating in coplanar circular orbits about their mutual barycenter.²⁰ Further, it is assumed that the spacecraft and the primary bodies are all point masses. The motion of the spacecraft in the CR3BP framework is derived in the context of a dextral orthonormal triad \hat{x}, \hat{y} and \hat{z} that constitutes a coordinate system, \mathbb{R} , rotating at a fixed rate, consistent with the revolution of the primary bodies about their barycenter. The \hat{x} axis in the rotating frame is the line joining the primaries, i.e., the Earth-Moon line; the positive direction is a view from the Earth towards the Moon. The direction normal to the Earth-Moon orbit plane and parallel to the orbital angular momentum is denoted by the positive \hat{z} direction. Finally, \hat{y} completes the right-hand coordinate system. The three spacial directions are used to describe the nonlinear spacecraft motion. The position vector is represented as $\bar{r} = [x, y, z]^T$ and velocity states by $\bar{v} = [\dot{x}, \dot{y}, \dot{z}]^T$. Again, for convenience, the 6-dimensional state is written by $\bar{\mathbf{x}} = [\bar{r}^T, \bar{v}^T]^T = [x, y, z, \dot{x}, \dot{y}, \dot{z}]^T$, where superscript 'T' implies a transpose operation. Note that overbars represent vector quantities. The CR3BP dynamics facilitates understanding of the underlying nonlinear spacecraft motion rather than direct analysis in the higher-fidelity ephemeris model due to time-dependency as well as additional complexities. The model in the CR3BP also admits five equilibrium points, all in the xy plane, labelled as the libration points, or Lagrange points. Identified as L1 through L5, the first three L1, L2 and L3 are collinear and located on the line joining the primary bodies. In the Earth-Moon system, the equilibrium point L1 lies on the \hat{x} -axis between the Earth and the Moon, while L2 is on the far side of the Moon.

An infinite number of periodic orbits exist in the CR3BP as limit cycles. The location, stability characteristics as well as the accessibility to the periodic orbits in the CR3BP system determine their suitability as potential mission candidates. Within the Earth-Moon system, a family of 3-dimensional periodic trajectories near the L1 and L2 equilibrium points, commonly termed halo orbits, are potential destinations for a long-term facility in cislunar space.²¹ Specifically for NASA's Gateway mission, an L2 southern halo orbit is the current focus. Some members of the L2 halo family with close lunar passages and high out-of-plane amplitudes are stable or nearly stable based on a variational linear stability analysis.¹ The stability index, $\nu_i = (1/2)(\lambda_i + 1/\lambda_i)$, is a parameter defined to measure the stability characteristics for a periodic orbit, where λ_i are the eigenvalues from the monodromy matrix, i.e., the state transition matrix computed over precisely one orbital period. For stable orbits, the absolute value of the stability index is less than or equal to one, i.e., $|\nu_i| \leq 1$. The Near Rectilinear Halo Orbits (NRHOs) are a subset of the halo orbit family that are stable or nearly stable orbits, as measured using stability index. The Distant Retrograde Orbits (DRO) and the Low Lunar Orbits (LLO) also offer a range of stable or nearly stable orbits.

STRETCHING DIRECTIONS

The maximum stretching direction at any point along an orbit is constructed to assess the impact of a maneuver. The spacecraft advances along a ballistic trajectory between two successive impul-

sive maneuver locations, for a time interval specified by the coast duration. A linear state transition matrix (STM) is generally reliable to assess the impact of deviations on the states at some time downstream. The linear flow is visualized using the Cauchy-Green tensor (CGT), a function of the STM, that offers reliable estimation of perturbation growth, especially for orbits where leveraging manifold structures may not be straightforward. The Cauchy-Green tensor (CGT), or simply ‘C’, is a product of the transpose (superscript T) of the state transition matrix (STM) defined as

$$\mathbb{C}(t_f, t_0) = \phi(t_f, t_0)^T \phi(t_f, t_0) \quad (1)$$

that renders the square of the magnitude of the final deformation to the initial deformation such that

$$\|\delta\bar{\mathbf{x}}_f\|^2 = \delta\bar{\mathbf{x}}_f^T \delta\bar{\mathbf{x}}_f = \delta\bar{\mathbf{x}}_0^T \phi(t_f, t_0)^T \phi(t_f, t_0) \delta\bar{\mathbf{x}}_0 = \delta\bar{\mathbf{x}}_0^T \mathbb{C}(t_f, t_0) \delta\bar{\mathbf{x}}_0. \quad (2)$$

where t_0 and t_f are the initial and final epochs while $\phi(t, t_0) = \frac{\partial \bar{\mathbf{x}}(t)}{\partial \bar{\mathbf{x}}_0}$ is the linear STM.^{22,23} The STM is evaluated on a reference trajectory, $\bar{\mathbf{x}}^*(t)$, to map the initial perturbed states, $\delta\bar{\mathbf{x}}_0$, to the final perturbed isochronous states, $\delta\bar{\mathbf{x}}_f$. The eigen-decomposition of the CGT, or the singular value decomposition of the STM, offers information about directions and magnitudes of the perturbation growth. The eigen-decomposition of the CGT field yields the eigenvalues λ_i and the eigenvectors \mathbb{V}_i , such that the contraction or expansion of the local phase space is represented by σ_i in the directions along \mathbb{V}_i . Here, $\sigma_i = \sqrt{\lambda_i}$. The singular value decomposition (SVD) of the STM,

$$\mathbb{U}\Sigma\mathbb{V}^* = \phi(t_f, t_0) \quad (3)$$

offers additional directional information, i.e., \mathbb{U} , also $\mathbb{U} = \phi(t_f, t_0)\mathbb{V}$. The columns of the matrix \mathbb{U} yield the stretching directions at the final epoch. For a square matrix, ϕ , Σ is a diagonal matrix with $\sigma_1 > \sigma_2 > \dots > \sigma_n$, where $\sigma_i = \Sigma_{ii}$, is the element in Σ located in the i^{th} row and i^{th} column. The principal stretching directions at time t_0 , along a propagated arc, is captured by the matrix \mathbb{V} . The matrices \mathbb{U} and \mathbb{V} are each orthonormal. Figure 1 illustrates the contraction and expansion along different flow directions using the example of a two-dimensional system transformed through CGT.

Different elements of the STM offer a correlation between a corresponding initial state and a final state. The flow between two successive impulsive maneuvers, at time t_0 and t_f respectively, is delivered by the STM evaluated along a ballistic segment, i.e., φ_C , such that

$$\varphi_C(t_f, t_0) = \begin{bmatrix} \varphi_{C,r,r} & \varphi_{C,r,v} \\ \varphi_{C,v,r} & \varphi_{C,v,v} \end{bmatrix} = \begin{bmatrix} \frac{\partial \bar{r}_f}{\partial \bar{r}_0} & \frac{\partial \bar{r}_f}{\partial \bar{v}_0} \\ \frac{\partial \bar{v}_f}{\partial \bar{r}_0} & \frac{\partial \bar{v}_f}{\partial \bar{v}_0} \end{bmatrix} \quad (4)$$

where $\varphi_{C,r,r}$, $\varphi_{C,r,v}$, $\varphi_{C,v,r}$ and $\varphi_{C,v,v}$ are the 3×3 submatrices of 6×6 matrix φ_C . Specific submatrices of φ_C yield more relevant characteristics. For example, the 3×3 dimensional submatrix, $\varphi_{C,r,v}$, maps the initial velocity perturbation, $\delta\bar{v}_0$, to the final position change, $\delta\bar{r}_f$, and the 3×3 dimensional submatrix, $\varphi_{C,v,v}$, maps the initial velocity perturbation, $\delta\bar{v}_0$, to the final velocity change, $\delta\bar{v}_f$. An efficient departing maneuver rapidly leaves the vicinity of the reference orbit with minimum propellant consumption. Since departure is characterized by a sufficient change in position and velocity quantities, the combined, 6×3 dimensional submatrix $\varphi_{C,r,v}$, where

$$\varphi_{C,r,v} = \begin{bmatrix} \varphi_{C,r,v} \\ \varphi_{C,v,v} \end{bmatrix} \quad (5)$$

maps the initial velocity perturbation, $\delta\bar{v}_0$, to the combined final position and velocity state change, $\delta\bar{r}_f$ and $\delta\bar{v}_f$, and offers more relevant characteristics. The sensitivity of the orbit states at the

final time to the initial velocity changes is measured by monitoring the magnitude of maximum stretching, σ_1 , corresponding to the $\varphi_{C,rv,v}$ submatrix. Any velocity change along the direction \mathbb{V}_i , evaluated on the submatrix $\varphi_{C,rv,v}$, offers the maximum change in the combined position and velocity state magnitude at the final time and, thus, an effective direction to depart the proximity of the reference orbit.

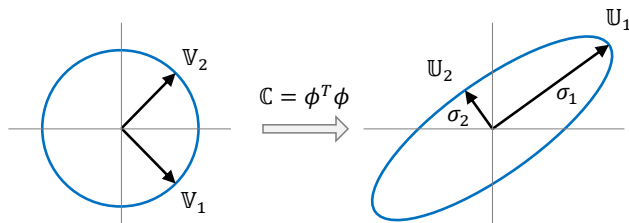


Figure 1: Principal stretching directions.

The orbit departure problem exploits any velocity change along the maximum stretching direction to rapidly deviate from the vicinity of the reference orbit. The application of the maneuver in the maximum stretching direction is antithesis to the stationkeeping problem demonstrated by Muralidharan and Howell,^{11,12,14} where effective stationkeeping maneuvers are delivered in the direction perpendicular to the maximum stretching direction to remain in the vicinity of the reference orbit.

ORBIT DEPARTURE

NASA's Gateway facility is to be maintained for a sufficiently long duration along the 9:2 synodic resonant orbit in the L2 southern NRHO family. The NRHO that is the current baseline is nearly stable. While a nearly stable orbit is suitable for reducing the stationkeeping costs,^{2,11,12,24} it is challenging to get the spacecraft and/or the discarded logistic modules away from the reference orbit²⁵ and avoid any potential collisions with the in-orbit spacecraft. This investigation focuses on leveraging the maximum stretching direction as a tool to depart the vicinity of a nearly stable NRHO and provide an alternative to exploiting manifolds for departure. Manifolds offer a suitable highway architecture to access and departure from the orbit, but for notably unstable orbits. As the stability of the orbit increases, the functionality of the manifolds reduces for such applications. The orbit departure problem in this investigation potentially serves as the preliminary step for disposals and transfers.

Momentum Integral

The Momentum integral is a parameter defined to identify the periodicity and boundedness of a trajectory.² Mathematically, it is the line integral of the position vector along a trajectory, i.e.,

$$\text{MI}(t) = \int_{t_0}^t x(\tau)\dot{x}(\tau) + y(\tau)\dot{y}(\tau) + z(\tau)\dot{z}(\tau)d\tau \quad (6)$$

where, the position vector is defined relative to the Earth-Moon barycenter in the CR3BP frame. For a time-invariant system such as the higher-fidelity ephemeris model where states are not precisely periodic, the momentum integral is not perfectly periodic, however, remains bounded along a trajectory that resembles the geometry of an orbit. The Momentum integral evaluated along trajectories in the neighborhood of the reference trajectory provides a suitable measurement to assess their boundedness. Figure 2(a) demonstrates the behavior of a perturbed trajectory, colored as red, relative to the reference trajectory, colored as black, in configuration space. Figure 2(b) quantifies the momentum integral evaluated along the trajectories in Figure 2(a). Clearly, the evolution of the momentum integral along the periodic reference path and the perturbed path are reflective of the motion in the configuration space. The reference trajectory is perfectly periodic, and the value of the momentum integral corresponds to the same behavior. However, the perturbed trajectory, colored in red, undergoes motion similar to the reference trajectory for a certain duration before departing

significantly from the reference motion. Consider, the reference trajectory represented by Γ , and the perturbed trajectory as $\tilde{\Gamma}$. A metric, defined as

$$\Delta MI(t) = |MI_{\tilde{\Gamma}}(t) - MI_{\Gamma}(t)| \quad (7)$$

that is, the absolute value of the difference between the momentum integral evaluated along the actual perturbed path and the reference path. This metric serves well to quantify the departure of the actual perturbed path relative to the reference path. Consistent with the previous literature as applied to an NRHO,²⁵ a spacecraft is considered to have departed the vicinity of the reference path if the value of ΔMI exceeds 10^{-1} , however, the specific value best suited for defining departure is dependent on each problem. For the current application, using 10^{-1} for the threshold is adequate. The departure of the perturbed trajectory, in Figure 2(a), is quantified relative to the reference trajectory in terms of ΔMI in Figure 2(c). Based on the assumed threshold, the ΔMI at the end of the propagated segment is larger than 10^{-1} , hence it is considered to have departed the vicinity of the reference NRHO.

Invariant manifolds have been leveraged extensively for trajectory design applications and disposal.^{26–31} Although manifold theory is effective for unstable orbits, relatively stable orbits do not possess well distinguished manifolds. Examples in this investigation are based on the baseline orbit under consideration for Gateway. The 9:2 synodic resonant L2 NRHO is "nearly" stable suggesting that unstable manifolds exist but are challenging

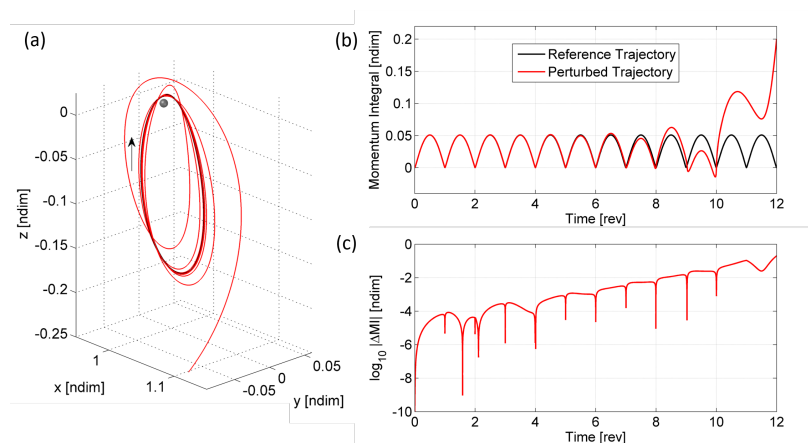


Figure 2: Detecting departure of neighboring trajectory. (a) Reference trajectory (black) and perturbed neighboring trajectory (red) is plotted in the configuration space. (b) Momentum integral value computed along the reference and perturbed trajectory. (c) Absolute difference between momentum integral of the perturbed trajectory relative to the reference.

to numerically construct, particularly near lunar vicinity. The unstable manifolds along the 9:2 synodic resonant southern L2 NRHO with an approximate perilune radius of 3200 km is plotted in Figure 3(a). An alternate strategy leverages maneuvers delivered in the maximum stretching direction. The two sets of maximum stretching directions labelled as type 'A' and type 'B' are plotted in Figures 3(b) and 3(c), respectively. For each of the plots in Figure 3 and throughout this investigation, locations along the NRHO are represented in terms of osculating true anomaly.¹² Departures along the unstable manifolds offer a criterion to identify the effectiveness of leveraging the maximum stretching directions. Trajectories along the unstable manifold directions are propagated for a duration of 10 revs of the reference NRHO, approximately equal to 65.73 days. These trajectories in configuration space are plotted in Figure 4(a), where the color for each trajectory corresponds to the osculating true anomaly location at which the states along the unstable manifolds are propagated. The corresponding absolute difference in the momentum integral evaluated along each of these trajectories relative to the reference NRHO are plotted in Figure 4(b). For reference, the threshold value of $\Delta MI = 10^{-1}$ is also displayed, to identify the departed trajectories. A simplified way of

classifying the departed trajectories is by identifying the time at which the trajectory exceeds the $\Delta MI = 10^{-1}$ criterion. Some departed trajectories may drop back below $\Delta MI < 10^{-1}$ values due to the underlying nonlinear motion, however, for simplicity, only the time at which the first departure condition is satisfied is recorded. Figure 5 reflects the time for the trajectories along the unstable manifold directions to be labelled departure. The blue and the red data points correspond to the two unstable manifold directions at a given osculating true anomaly location along the orbit. For certain osculating true anomaly values, either one or no data points are recorded, indicating that either one or none of the unstable manifolds propagated from that value of true anomaly departs the vicinity of the NRHO for the propagated time duration, respectively. In general, for most true anomaly values, a trajectory along the unstable manifold direction requires at least 50 days to be considered departed.

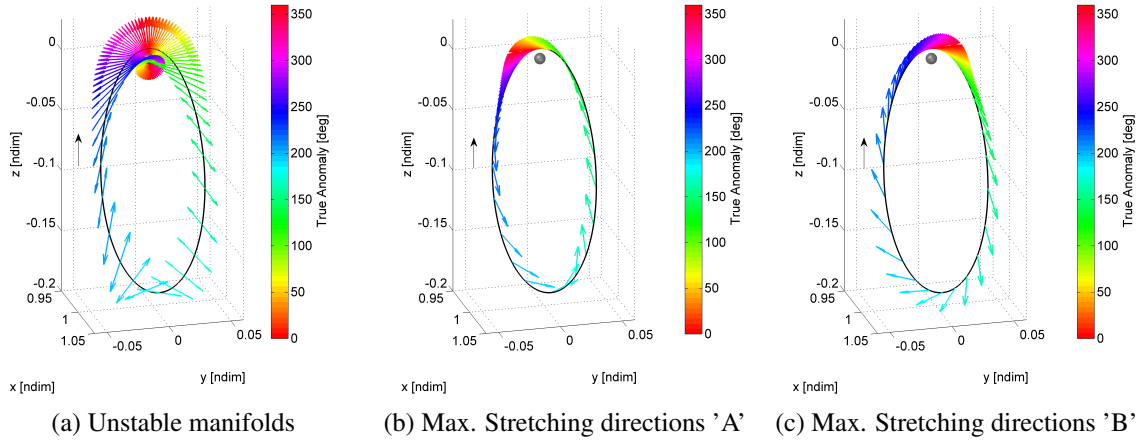


Figure 3: Unstable manifold directions and maximum stretching directions along the 9:2 synodic resonant southern L2 NRHO.

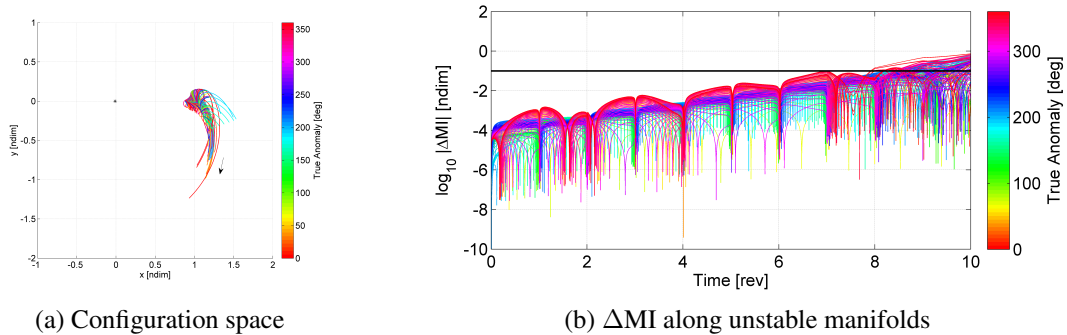


Figure 4: Trajectories along unstable manifolds in the configuration space, and their corresponding ΔMI values.

A maneuver along the maximum stretching direction impacts the maximum change in the magnitude of the state at the end of the propagated arc. In most applications, within trajectory design or for disposal, a specific time duration for the propagation may be unknown *a priori*. For simplicity, the maximum stretching directions are computed along with the monodromy matrix. The maximum stretching direction leveraging the monodromy matrix, inherently assumes that a delivered maneuver causes a sufficient step-off and consequently gets captured along other manifold structures, resonant arcs and sections of higher periodic orbits. Such structures aid in rapid departure from the stable orbit.

In contrast to leveraging the unstable manifolds, an actual maneuver is delivered along the maximum stretching direction, for different locations on the NRHO. Similar to the unstable manifolds, there exists two sets of maximum stretching directions, labelled as type 'A' and type 'B', as demonstrated in Figures 3(b) and 3(c), respectively. Initial maneuvers of different magnitude results in different variations in the final state. Figures 6(a), 6(c), 6(e) and 6(g) demonstrate the effect of maneuvers of magnitudes 1 m/s, 4 m/s, 16 m/s and 100 m/s as viewed in configuration space. In these figures, maneuvers are delivered along the maximum stretching directions as indicated in both type 'A' and type 'B'. Note that the Jacobi constant along the unstable manifolds is consistent with the reference NRHO, however, with the delivery of an additional maneuver along the maximum stretching direction, the Jacobi constant for the perturbed trajectory is no longer precisely the same as the reference orbit. Thus, the Jacobi constant or the energy level along the trajectory in the Type 'A' direction and Type 'B' direction at the corresponding osculating true anomaly location may be different. An increase or decrease in the energy level of the trajectory does not correlate directly to the rate of departure. The change in the momentum integral evaluated along each of the perturbed trajectories, ones with maneuvers along the maximum stretching directions, given in Figures 6(b), 6(d), 6(f) and 6(h) for maneuver magnitudes of 1 m/s, 4 m/s, 16 m/s and 100 m/s, respectively, offers a better assessment of the actual orbital departures. The direction of the implemented maneuver, i.e., type 'A' or type 'B' directions are more important in identifying departing trajectories along with the magnitude of the maneuvers. Similar to identifying the time for departure for unstable orbits as in Figure 5, the time at which the departure conditions are satisfied are also recorded for trajectories that incorporate maneuvers delivered along the maximum stretching directions. Figures 7(a), 7(b), 7(c) and 7(d), correspond to the times to depart, for cases with maneuver magnitudes of 1 m/s, 4 m/s, 16 m/s and 100 m/s, respectively. These times correspond to the first instance when the $|\Delta MI|$ value exceeds the 10^{-1} value as illustrated in Figures 6(b), 6(d), 6(f) and 6(h), respectively. In Figure 6(b), maneuvers of magnitude 1 m/s delivered along type 'A' (colored in blue) and type 'B' (colored in red) directions, and across different location on the NRHO are successful in departing over the propagated duration. Certain trajectories depart as rapidly as 7 days after the onset of the propagation, while most of the trajectories depart within 50 days of the initiation of propagation. Such departure times are easily assessed in comparison to departure along the unstable manifold that require at least 50 days to depart. Type 'A' directions are loosely aligned away from the orbit velocity directions while type 'B' directions includes significant components in the velocity direction. With an increase in the maneuver magnitudes, the behavior of the trajectories along the type 'A' and type 'B' maneuver directions bifurcate. For a significantly large maneuver magnitude of 100 m/s, as in Figure 7(d), most trajectories along the type 'A' direction do not depart the NRHO vicinity in the propagated time duration. By virtue of the direction of maneuver, a loss in energy results in the trajectories remaining captured in the lunar vicinity, rather than the broader Earth-Moon space. Even trajectories propagated with a 100 m/s maneuver magnitude along the type 'A' direction, for departure locations near the Moon, remain in Lunar orbits as illustrated in Figure 8. In contrast, the maneuvers along type 'B' directions elevates the rate of departure, and most trajectories depart within 10 days of propagation. Especially for larger maneuver magnitudes, the stark contrast between the behavior of trajectories after maneuvers are delivered in type 'A' and type 'B' directions, are evident in Figure 6(h). The $|\Delta MI|$ value for trajectories that leverage type 'A' maneuver directions offer periodic behavior and boundedness, while $|\Delta MI|$ value for trajectories that

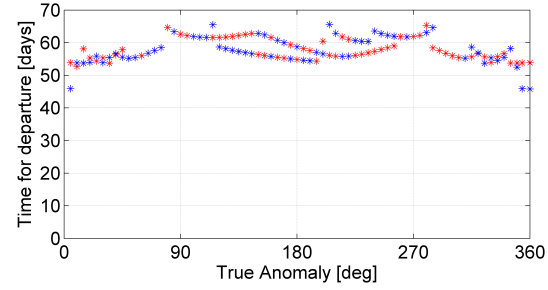
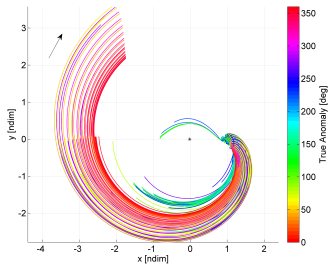


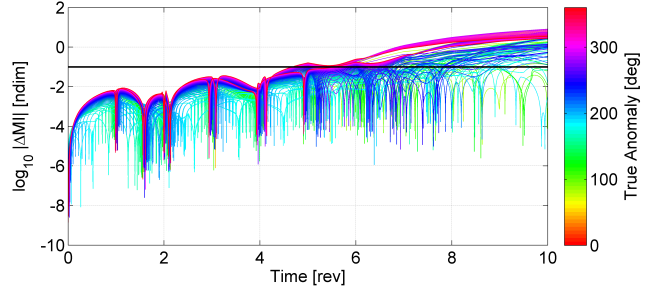
Figure 5: Time to depart along unstable manifolds

Figure 5, the time at which the departure conditions are satisfied are also recorded for trajectories that incorporate maneuvers delivered along the maximum stretching directions. Figures 7(a), 7(b), 7(c) and 7(d), correspond to the times to depart, for cases with maneuver magnitudes of 1 m/s, 4 m/s, 16 m/s and 100 m/s, respectively. These times correspond to the first instance when the $|\Delta MI|$ value exceeds the 10^{-1} value as illustrated in Figures 6(b), 6(d), 6(f) and 6(h), respectively. In Figure 6(b), maneuvers of magnitude 1 m/s delivered along type 'A' (colored in blue) and type 'B' (colored in red) directions, and across different location on the NRHO are successful in departing over the propagated duration. Certain trajectories depart as rapidly as 7 days after the onset of the propagation, while most of the trajectories depart within 50 days of the initiation of propagation. Such departure times are easily assessed in comparison to departure along the unstable manifold that require at least 50 days to depart. Type 'A' directions are loosely aligned away from the orbit velocity directions while type 'B' directions includes significant components in the velocity direction. With an increase in the maneuver magnitudes, the behavior of the trajectories along the type 'A' and type 'B' maneuver directions bifurcate. For a significantly large maneuver magnitude of 100 m/s, as in Figure 7(d), most trajectories along the type 'A' direction do not depart the NRHO vicinity in the propagated time duration. By virtue of the direction of maneuver, a loss in energy results in the trajectories remaining captured in the lunar vicinity, rather than the broader Earth-Moon space. Even trajectories propagated with a 100 m/s maneuver magnitude along the type 'A' direction, for departure locations near the Moon, remain in Lunar orbits as illustrated in Figure 8. In contrast, the maneuvers along type 'B' directions elevates the rate of departure, and most trajectories depart within 10 days of propagation. Especially for larger maneuver magnitudes, the stark contrast between the behavior of trajectories after maneuvers are delivered in type 'A' and type 'B' directions, are evident in Figure 6(h). The $|\Delta MI|$ value for trajectories that leverage type 'A' maneuver directions offer periodic behavior and boundedness, while $|\Delta MI|$ value for trajectories that

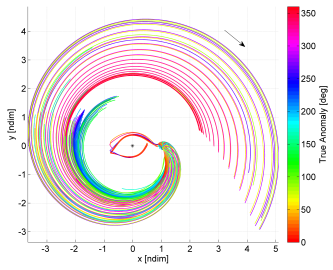
leverage type 'B' maneuver directions increase rapidly before approaching an asymptotic behavior as the spacecraft continuously deviates away from the Earth-Moon vicinity in a spiral behavior as observed in the rotating frame of view.



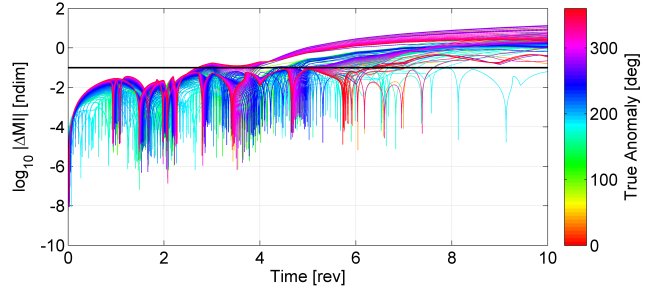
(a) Configuration space ($|\Delta\bar{v}| = 1$ m/s)



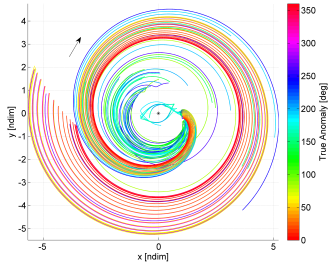
(b) ΔMI along trajectories after $|\Delta\bar{v}| = 1$ m/s maneuver



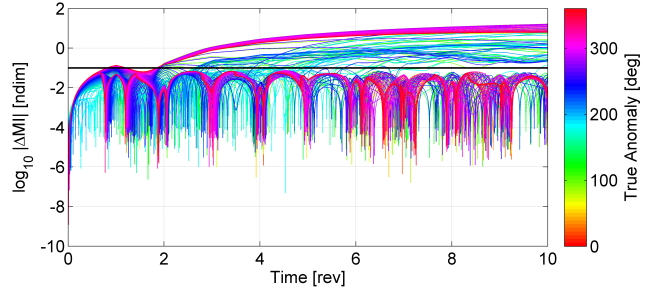
(c) Configuration space ($|\Delta\bar{v}| = 4$ m/s)



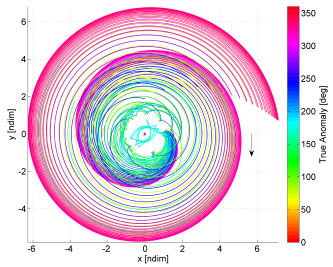
(d) ΔMI along trajectories after $|\Delta\bar{v}| = 4$ m/s maneuver



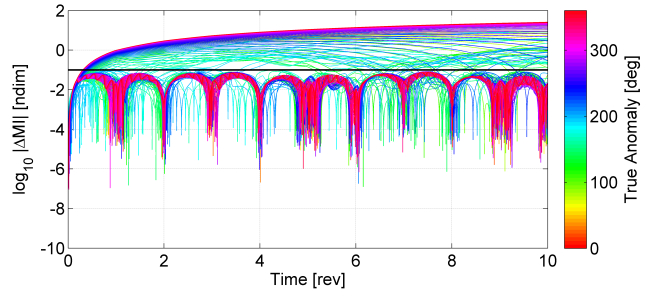
(e) Configuration space ($|\Delta\bar{v}| = 16$ m/s)



(f) ΔMI along trajectories after $|\Delta\bar{v}| = 16$ m/s maneuver



(g) Configuration space ($|\Delta\bar{v}| = 100$ m/s)



(h) ΔMI along trajectories after $|\Delta\bar{v}| = 100$ m/s maneuver

Figure 6: Trajectories in configuration space after maneuver along most stretching direction, and their corresponding ΔMI values.

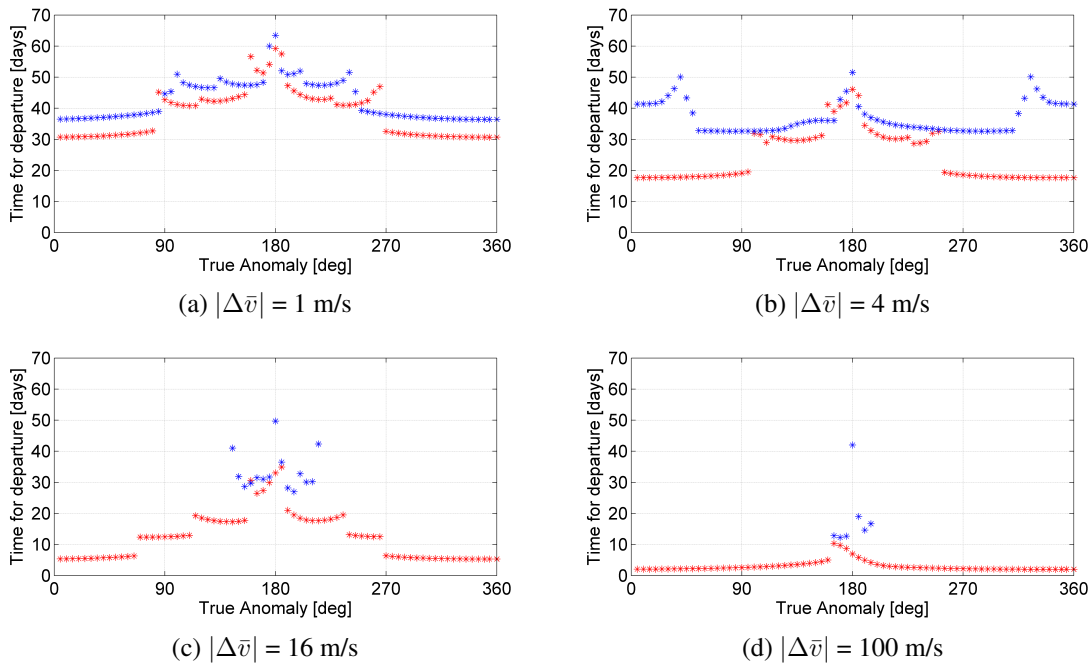


Figure 7: Time to departure for trajectories perturbed from the reference NRHO with maneuvers of different magnitudes. Blue asterisks (*) corresponds to direction type 'A' while red asterisks (*) to type 'B'.

Maneuvers along velocity, normal and co-normal (VNC) directions to assist in departure are investigated by Davis et al.³² Maneuvers delivered along the rotating velocity directions for the NRHO, implemented close to the periapsis region, offers faster departure.³² Similar results are observed in this investigation, where maneuvers delivered along the type 'B' directions, aligned close to the rotating velocity direction, is more conducive to rapid departure. Maximum stretching direction type 'B' are correlated with rapid departure relative to type 'A', however, for smaller maneuver magnitudes even type 'A' directions can offer departure with marginally larger times of flight.

TRANSFER TRAJECTORY DESIGN

The ability to depart an orbit serves as a preliminary step to design transfers between two regions in space. In a nonlinear system it is challenging to determine the initial states that drive the spacecraft to the desired final location. Transfers between stable regions in space have utilized intermediate arcs of known orbits, including resonant orbits, as well as the underlying manifold structures of nearby unstable orbits. In the nonlinear CR3BP, there are numerous solutions that may offer suitable options for transfers, however, a preliminary notion of the most productive types of intermediate orbits is nontrivial. Furthermore, transfer options are most likely restricted to evolve along the underlying structures that are incorporated. Direct transfers that employ a shooting algorithm to transfer between orbits are also offered in the literature, however, a suitable initial

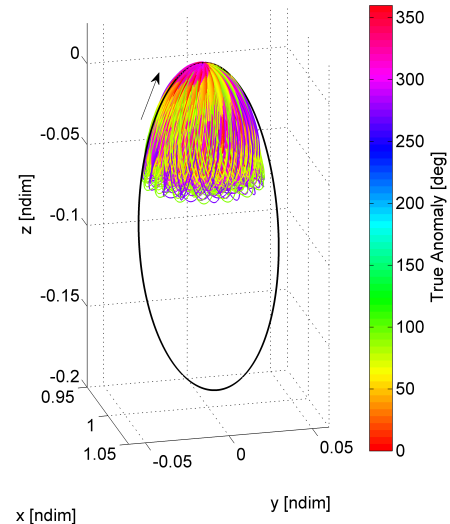


Figure 8: Trajectories captured near Moon vicinity

guess for the shooting algorithm may not be intuitive. Thus, the application of direct transfers may be restricted to orbits that are nearby in configuration space. In addition, incorporating only two maneuvers along the transfer arc, i.e., a departure and an arrive maneuver may not necessarily be the most cost-effective option. Maps offer useful information to bridge this challenge by reducing the number of free variables. The primary motivation of this investigation is a demonstration of maximum stretching direction as a tool to assist in transfer trajectory design. In this investigation, for stable orbits, in the absence of well-defined unstable and stable manifold structures, maneuvers are delivered along the maximum stretching directions and the updated states are propagated until a pre-selected hyperplane crossing. Selection of an hyperplane is application-specific. For maps in this investigation, position and velocity states at the hyperplane crossings are recorded. Velocity components may be included in terms of glyphs if necessary,^{33,34} however, glyphs are not included in this work. A combination of trajectory crossings and manifold crossings are also an option subject to the type of departure and arrival orbit and their stability characteristics. It is desirable for the transfer trajectory design process to determine an appropriate combination of crossings for the departure arcs and the arrival arcs at the hyperplane, with small discontinuities in the position and velocity states. An optimization scheme is introduced to generate a continuous transfer between the departure orbit and the arrival orbit that leverages the departure and arrival arc determined from the map.¹⁴ A schematic representation of the transfer trajectory optimization process is illustrated in Figure 9. For reference, the orbit colored in cyan is the departure orbit while orbit in magenta is the arrival orbit. The intermediate departure and arrival arcs are colored in blue and red, respectively. In this investigation, the transfer design process employs three impulsive maneuvers, i.e., $\Delta\bar{v}_{dep}$ to transition from the departure orbit to the departure arc, an intermediate maneuver, $\Delta\bar{v}_{int}$, to progress from the departure arc to the arrival arc, and finally $\Delta\bar{v}_{arr}$ to transition from the arrival arc to the arrival orbit. An optimization scheme minimizes the cost function, J , such that

$$\min J = |\Delta\bar{v}_{dep}| + |\Delta\bar{v}_{int}| + |\Delta\bar{v}_{arr}| \quad (8)$$

$$= \sqrt{\Delta\bar{v}_{dep}^T \Delta\bar{v}_{dep}} + \sqrt{\Delta\bar{v}_{int}^T \Delta\bar{v}_{int}} + \sqrt{\Delta\bar{v}_{arr}^T \Delta\bar{v}_{arr}} \quad (9)$$

i.e., the sum of total maneuver magnitudes, $|\Delta\bar{v}|$. Here,

$$\Delta\bar{v}_{dep} = \bar{v}_{dep-arc}(t=0) - \bar{v}_{dep-orbit}(t=\tau_1) \quad (10)$$

$$\Delta\bar{v}_{int} = \bar{v}_{arr-arc}(t=0) - \bar{v}_{dep-arc}(t=ToF_{dep}) \quad (11)$$

$$\Delta\bar{v}_{arr} = \bar{v}_{arr-orbit}(t=\tau_2) - \bar{v}_{arr-arc}(t=ToF_{arr}) \quad (12)$$

such that ToF_{dep} is the time of flight along the departure arc prior to $\Delta\bar{v}_{int}$, while ToF_{arr} is the time of flight along the arrival arc after $\Delta\bar{v}_{int}$ and prior to $\Delta\bar{v}_{arr}$. The total time of flight for the transfer is the sum of ToF_{dep} and ToF_{arr} . The initial and the final position states are constrained to remain on the departure and arrival orbits, respectively. In the optimization process, the departure and the arrival position states are free to advance

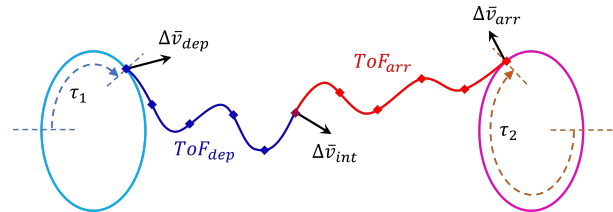


Figure 9: Schematic for transfer trajectory optimization.

along the orbit and may differ from the initial guess. To constrain the departure and the arrival position states on the orbit, an additional τ constraint is incorporated, such that τ_1 and τ_2 are certain time durations from a fixed location along the departure and arrival orbits, respectively. Locally optimal solutions are generated that resemble the geometry predicted by the initial guess.

Transfers between L2 Southern 9:2 Synodic Resonant NRHO to L2 Northern 9:2 Synodic Resonant NRHO

The 9:2 synodic resonant orbit in the southern and northern L2 NRHO families are a current focus for various mission scenarios, primarily due to close passages near the polar regions of the Moon and the relatively stable nature of the orbit. A transfer between the two stable orbits is designed using maneuvers delivered along the maximum stretching directions. Due to very small unstable eigenvalue for the flow along these NRHOs, the rate of departure is very low. As observed in Figure 5, leveraging manifold structures may take a significantly longer duration to depart and the numerical eigenvectors may not be precisely accurate. Maneuvers are delivered along the maximum stretching direction at various locations along the orbit, measured in terms of an osculating true anomaly.^{11,12} Maneuvers of fixed magnitude are delivered along both sets of maximum stretching directions, type 'A' and type 'B', and the updated states are propagated for a significantly long duration. These trajectories intersect with the selected hyperplanes on multiple occasions. Each crossing at the hyperplane is recorded to generate a comprehensive map. For the transfer between the L2 southern 9:2 synodic resonant NRHO and the L2 northern 9:2 synodic resonant NRHO, two different hyperplanes are considered, the xy -plane and the xz -plane. The 2-sided plane crossings are recorded, i.e., in the positive and the negative velocity directions. Figure 10(a) demonstrates the crossings of each of these trajectories propagated from various locations along the NRHO orbits to the $z = 0$ hyperplane, i.e., on the xy plane. Similarly, Figure 10(b) demonstrates the crossings on the $y = 0$ hyperplane, i.e., on the xz plane. Blue asterisks (*) correspond to the crossings along the departure arcs that are propagated from the 9:2 synodic resonant L2 southern NRHO forwards in time, while red asterisks (*) correspond to crossings along arrival arcs from the 9:2 synodic resonant L2 northern NRHO that are propagated backwards in time. Along a forward propagated segment, the maximum stretching directions are computed from the submatrix of the monodromy matrix, i.e., the matrix $\varphi_{C,r,v,v}(\varphi, 0)$. In contrast, for a backwards propagated segment, the maximum stretching directions are computed from the submatrix $\varphi_{C,r,v,v}(0, \varphi)$. Here, φ is the time period corresponding the 9:2 synodic resonant southern and northern L2 NRHO. Common practise for transfer trajectory design is to transition from the departure arc to the arrival arc at the hyperplane. Thus, an appropriate choice is the selection of the combination of a departure crossing and an arrival crossing on the hyperplane with a small state change, in position and velocity. The maps in Figure 10 are generated by propagating departure arc and arrival arc following departure and arrival maneuvers of size $|\Delta\bar{v}| = 1$ m/s. Maps that result from other $|\Delta\bar{v}|$ values also offer conducive transfers. Besides, the $|\Delta\bar{v}|$ value along the departure arc and the arrival arc need not be of the same magnitude. In the case of transfers between southern and northern NRHO of the same size, the $|\Delta\bar{v}|$ value along the departure arc and the arrival arc are the same to exploit the underlying similarity and symmetry in the maps.

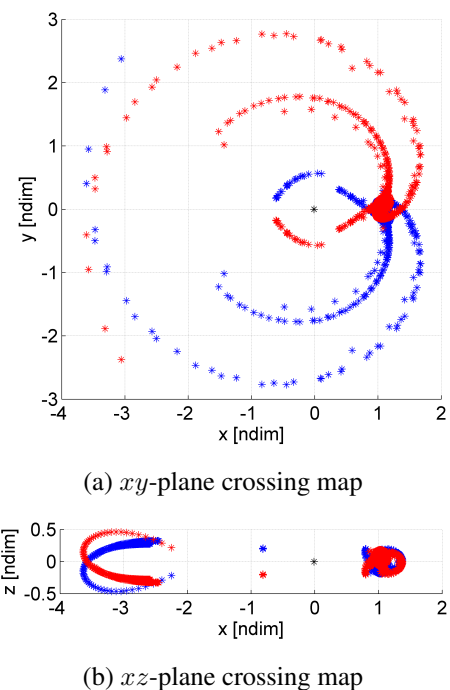


Figure 10: Two sided plane crossing maps. Blue asterisks (*) correspond to departure arcs from southern NRHO propagated forwards in time, while red asterisks (*) correspond to arrival arcs from northern NRHO propagated backwards in time. Map for $|\Delta\bar{v}| = 1$ m/s.

Combinations of departure and arrival arc crossings on the maps, as in Figure 10, and near the Moon offer interior transfers, i.e., loosely characterized by the trajectory remaining in the proximity of the region of interest.³⁵ Of course, several combinations of departure and arrival arcs are possible. These combinations offer reliable initial guesses for transfer trajectory design. The combination of departure and arrival crossings on the maps may not be continuous in position and velocity. An optimization scheme, as illustrated previously, is adopted to generate a continuous transfer with three maneuvers, $\Delta\bar{v}_{dep}$, $\Delta\bar{v}_{int}$ and $\Delta\bar{v}_{arr}$. Figures 11 and 12 are examples of locally optimal interior transfers that possess similar geometry in configuration space (although constructed from distinct initial guesses) but with marginally different times of flight. A different geometry for a transfer that exploits motion along the L1 axial orbit is produced in Figure 13. Figure 14 offers another geometry for a transfer with multiple loops on the L1 and L2 side of the Moon. The initial guess for each of the locally optimal interior transfers in Figures 11, 12, 13 and 14 are identified from the map in Figure 10(a) that is generated based of departure and arrival maneuver magnitudes of 1 m/s. Of course, bridging the gap in the state vector on the map, the optimal maneuvers, $|\Delta\bar{v}_{dep}|$ and $|\Delta\bar{v}_{arr}|$, may not precisely the initial guess, i.e., 1 m/s. Cases with small position and velocity discontinuities on the hyperplane crossing maps yield locally optimal solutions that are relatively close to the initial guess. In contrast, cases where the departure and arrival crossings on the map that possess larger discontinuity require larger maneuvers. The maneuver costs, as well as the times of flight for each of the transfers in Figures 11, 12, 13 and 14, are detailed in Table 1. The osculating true anomaly locations along the departure and arrival orbits for the locally optimal transfers are also listed in Table 1.

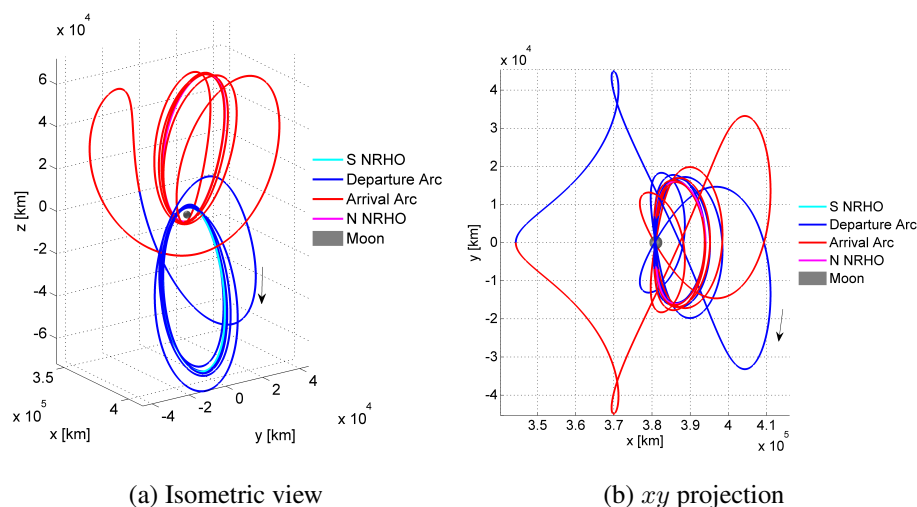


Figure 11: Optimal transfer between L2 southern 9:2 synodic resonant NRHO to L2 northern 9:2 synodic resonant NRHO (Case 1).

Trajectories that depart the proximity of interests are loosely characterized as exterior transfers.³⁵ Hyperplane crossing maps similar to Figure 10 are generated for departure and arrival maneuvers of magnitude of 20 m/s, aligned in the maximum stretching directions for types 'A' and 'B'. Of course, maps for other maneuver magnitudes may also offer a range of transfer trajectory options. On the $y = 0$ hyperplane map in Figure 10, i.e., the xz plane crossing map, a combination of departure and arrival arc crossings are apparent in the negative x -direction. One set of such crossings is now selected, one with relatively low position and velocity discontinuity. The selected combination of departure and arrival arc crossing offers an initial guess that is optimized, to reduce maneuver costs

and determine a trajectory continuous in position. Figure 15(a) is a locally optimal transfer between the 9:2 synodic resonant southern L2 NRHO to the 9:2 synodic resonant northern L2 NRHO that leverages an exterior type transfer. The transfer includes a single loop geometry around the Earth-Moon system. Yet another combination of departure and arrival arc crossings with a positive x -component are selected on the $y = 0$ hyperplane map, i.e., xz plane crossing map, with a relatively low position and velocity discontinuity. The initial guess is optimized to deliver a locally optimal transfer trajectory as plotted in Figure 15(b). The optimal trajectory incorporates a double loop geometry around the Earth-Moon system in contrast to single loop geometry for the optimal transfer in Figure 15(a). Not surprisingly, the time of flight for the transfer in Figure 15(b) is longer, however, the overall maneuver costs for both exterior type transfers demonstrated here are comparable. The details of the maneuver costs, times of flight and the osculating true anomaly for the departure and arrival locations on the corresponding orbits are summarized in Table 1. The exterior type transfers are generated from 20 m/s maneuvers delivered along the maximum stretching directions, therefore, trajectories depart or arrive the vicinity of the NRHOs more rapidly and sometimes offer shorter transfer time options. The times of flight and the maneuver costs associated with the transfers are influenced heavily by the combinations selected on the hyperplane crossing maps rather than the initial guess for the departure and arrival maneuver magnitudes alone. Since the 9:2 synodic resonant southern and northern NRHO possess the same energy, in theory, a ballistic transfer may exist.³⁵

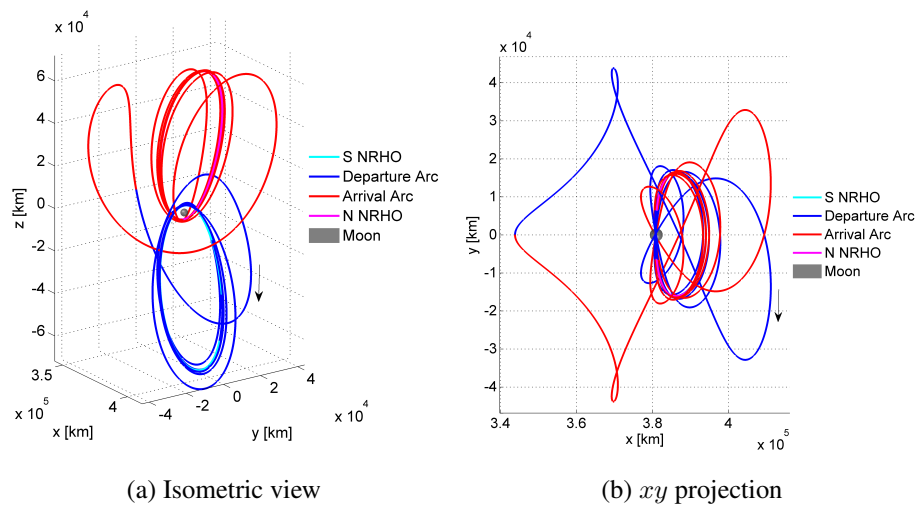


Figure 12: Optimal transfer between L2 southern 9:2 synodic resonant NRHO to L2 northern 9:2 synodic resonant NRHO (Case 2).

An infinitely many transfer trajectory design options are possible, both interior type and exterior type, and different transfer types can adapt to various constraints. Different combinations of departure and arrival arc crossings on different hyperplanes offer different solutions. In addition, various magnitudes for departure and arrival maneuvers alter the hyperplane crossing maps, yielding alternate solutions. The examples in this investigation demonstrate the capability of leveraging the maximum stretching directions for transfer trajectory design to transition between relatively stable orbits. Some of the transfer geometries are consistent with low-thrust transfers available in the literature, along with some that leverage resonant structures.^{6, 7, 35, 36}

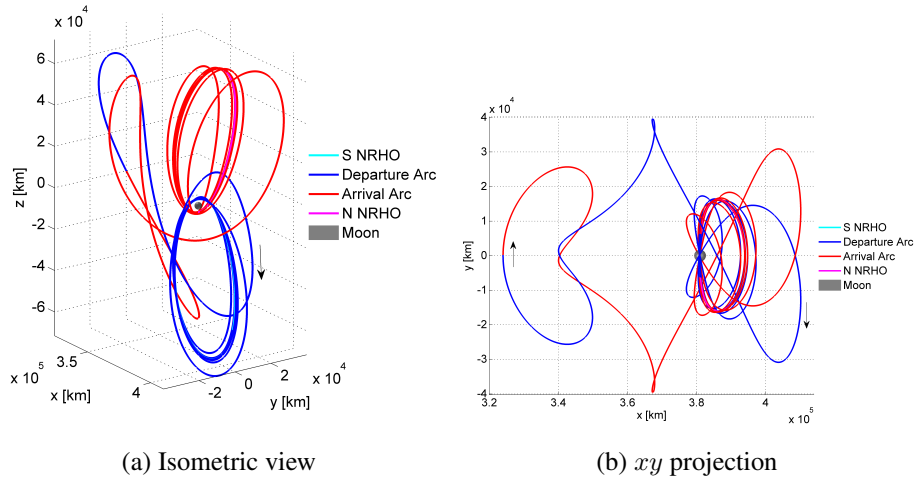


Figure 13: Optimal transfer between L2 southern 9:2 synodic resonant NRHO to L2 northern 9:2 synodic resonant NRHO (Case 3).

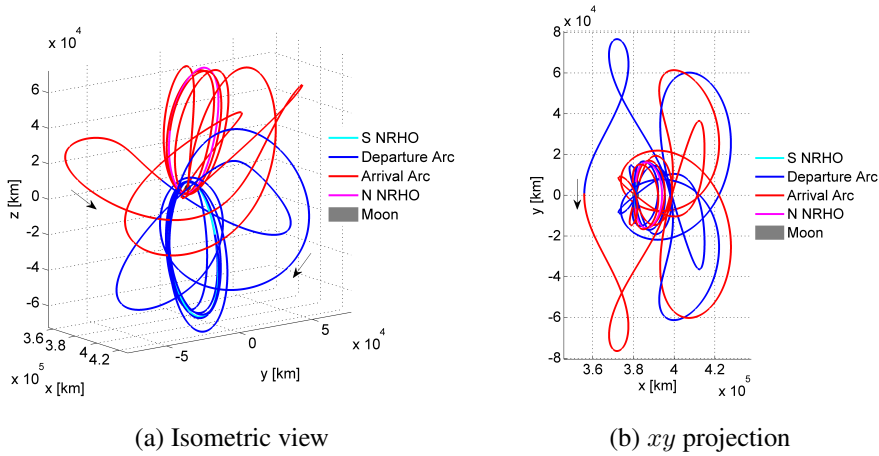


Figure 14: Optimal transfer between L2 southern 9:2 synodic resonant NRHO to L2 northern 9:2 synodic resonant NRHO (Case 4).

Transfers between L2 Southern 9:2 Synodic Resonant NRHO to Distant Retrograde Orbit (DRO)

The Lunar Distant Retrograde Orbits are also an interesting possibility for upcoming missions, primarily due to their proximity to the Moon and the stable nature of the orbits. Here, a transfer between the two nearly stable orbits, the 9:2 synodic resonant southern L2 NRHO and the 70,000 km Lunar DRO, are leveraged using initial guesses from maneuvers delivered along the maximum stretching directions. The DRO periapsis distance is 70,000 km from the Moon, measured along the x -axis towards the Earth. The orbit is defined by a time period of 13.934 days, a Jacobi constant value of 2.929 and are linearly stable with stability indices of -0.717, 0.107 and 1. Similar to the southern NRHO to northern NRHO transfers, a map is generated with maneuvers that are delivered along the maximum stretching directions at various locations along the orbit. For the DRO, due to the relatively consistent angular rate of rotation along the orbit measured with respect to the Moon, define an angle κ as the fraction of the time along the orbit relative to a fixed reference

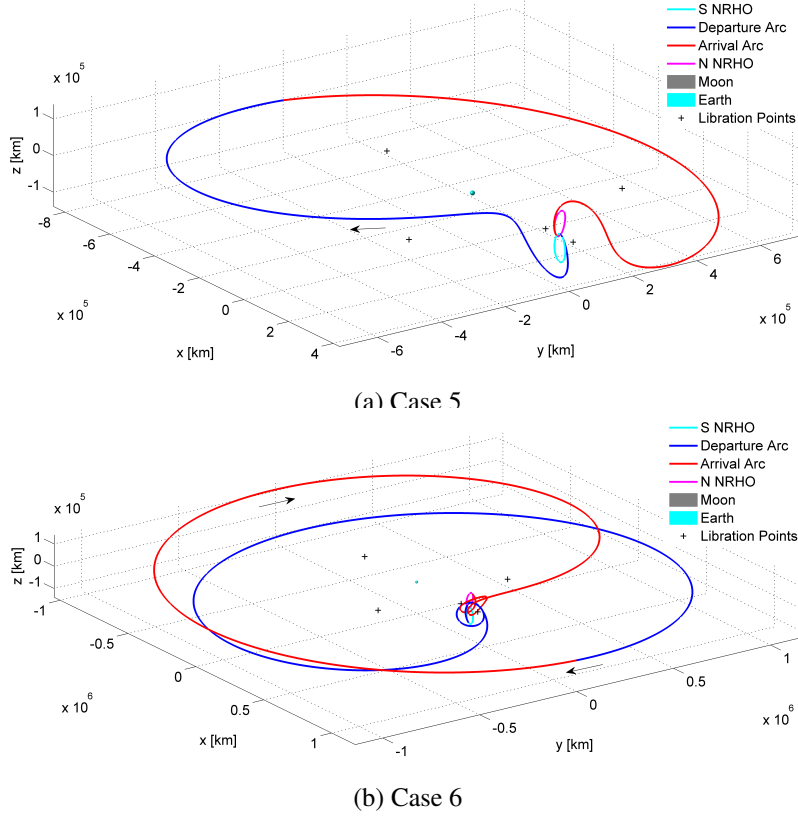


Figure 15: Optimal transfer between L2 southern 9:2 synodic resonant NRHO to L2 northern 9:2 synodic resonant NRHO.

(i.e., the periaapsis direction in the negative x -direction) and serves as a simple metric to determine the spacecraft location along the orbit. Maneuvers of fixed magnitudes are delivered along both sets of maximum stretching directions, type 'A' and type 'B', for both the NRHO and the DRO, and the updated states are propagated for a significantly long duration. The DRO is planar, thus, all the states lie in the xy plane. A $z = 0$ hyperplane, i.e., the xy plane, is incorporated with all trajectories emerging from the DRO propagated backwards in time, and all the xy plane crossings for the trajectories emerging from the NRHO propagated forwards in time. A semi-automated scheme determines a departure arc and an arrival arc at the hyperplane crossing.¹⁴ Within a region of interest on the map, the algorithm solves for the value of

$$\mathcal{J} = \left\| \begin{bmatrix} \alpha \Delta \bar{r} \\ (1 - \alpha) \Delta \bar{v} \end{bmatrix} \right\|$$

for each combination of departure and arrival states on the hyperplane. A combination that minimizes the value of \mathcal{J} is preferred. Here, $\Delta \bar{r}$ and $\Delta \bar{v}$ are the position and velocity discontinuities between the departure arc and the arrival arc at the hyperplane crossing, while α is a scaling factor to selectively control the position and velocity discontinuity. For crossings that are further from the primary bodies, the optimization algorithm compensates for a relatively larger position error, hence, a relatively smaller $\alpha \in [0.5, 0.9]$ is used. For crossings that are closer to the primary bodies, a smaller position discontinuity is essential for the optimization algorithm, hence a value of $\alpha \geq 0.9$ is favorable. Multiple maps are generated by propagating departure arcs and arrival arcs following maneuvers of various $|\Delta \bar{v}|$ sizes; an example appears in Figure 16. Different combinations of the departure and the arrival crossings on the maps offer different transfer geometries.

Table 1: Optimal transfers between 9:2 synodic resonant southern L2 NRHO to 9:2 synodic resonant northern L2 NRHO.

Parameter	Case 1	Case 2	Case 3	Case 4	Case 5	Case 6
	Figure 11	Figure 12	Figure 13	Figure 14	Figure 15(a)	Figure 15(b)
$ \Delta\bar{v}_{dep} $ [m/s]	3.59	2.05	0.88	10.12	27.32	112.34
$ \Delta\bar{v}_{int} $ [m/s]	0.00	0.00	0.00	0.00	188.55	0.00
$ \Delta\bar{v}_{arr} $ [m/s]	3.59	2.27	0.88	10.04	27.39	112.36
$ \Delta\bar{v}_{Total} $ [m/s]	7.18	4.33	1.76	20.17	243.25	224.70
ToF _{dep} [days]	50.08	54.95	61.10	62.35	36.99	58.44
ToF _{arr} [days]	50.08	54.68	61.07	62.19	36.99	58.43
ToF _{Total} [days]	100.16	109.62	122.17	124.54	73.98	116.87
TA_{dep} [deg]	175.52	154.68	164.57	148.27	67.13	193.02
TA_{arr} [deg]	174.84	201.88	195.39	207.49	292.59	166.97

Certain combinations of the departure and arrival arc crossings on the hyperplane that are near the Moon, as in Figure 16, offer interior type transfers. There are infinitely many combinations of departure and arrival arcs that are possible. A selected combination offers a reliable initial guess for transfer trajectory design between the NRHO and the DRO. An optimization scheme generates a continuous transfer with three maneuvers, $\Delta\bar{v}_{dep}$, $\Delta\bar{v}_{int}$ and $\Delta\bar{v}_{arr}$. Figures 17(a), 17(b) and 17(c) are examples of locally optimal interior transfers where the spacecraft remains in the Lunar vicinity. The initial guess corresponding to Figure 17(a) is extracted from a map generated by propagating trajectories from the NRHO with a maneuver of magnitude 1 m/s along the maximum stretching directions; similarly trajectories are propagated backwards in time from the DRO along the maximum stretching direction with a maneuver of 1 m/s. Figure 17(b) is an outcome from the map corresponding to maneuvers of magnitude 5 m/s and 20 m/s delivered on the NRHO and the DRO, respectively. Finally, a map with a maneuver magnitude of 20 m/s delivered on both the NRHO and the DRO, yields a geometry that resembles Figure 17(c). As stated previously, the optimal maneuvers, $|\Delta\bar{v}_{dep}|$ and $|\Delta\bar{v}_{arr}|$, are not precisely the same as the initial guesses, nor necessarily precisely aligned along the maximum stretching directions. The maneuver costs, as well as the time of flight for each of the transfers in Figure 17 are listed in Table 2. The osculating true anomaly locations along the departure NRHO, and the location corresponding to angle κ on the arrival DRO for the locally optimal transfers are also listed. For the transfers between two NRHOs that are similar in energy levels, a

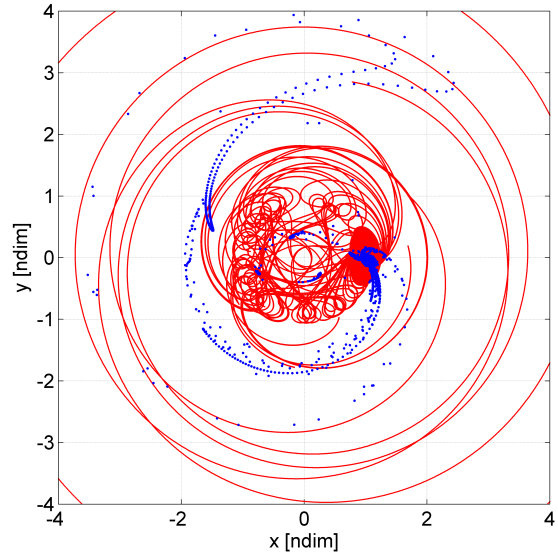


Figure 16: Two sided plane crossing maps. Blue dots (.) correspond to departure arc crossings from southern NRHO propagated forwards in time with $|\Delta\bar{v}| = 5$ m/s, while red dots (.) correspond to arrival arcs from DRO propagated backwards in time with $|\Delta\bar{v}| = 20$ m/s.

ballistic transfer may exist, however, for the transfer between the 3200 km L2 NRHO and the 70,000 km DRO, each possessing a different energy level, a ballistic transfer does not exist. A theoretical minimum $|\Delta\bar{v}|$ is required to raise the energy level from the NRHO to meet the energy level for the DRO. A theoretical minimum $|\Delta\bar{v}|$ is calculated, such that $|\Delta\bar{v}| = 35.48$ m/s must be delivered at the periapsis of the NRHO or $|\Delta\bar{v}| = 261.86$ m/s at the apoapsis of the NRHO to meet the energy level for the DRO.^{7,14}

Intersections of the departure and arrival arcs on the hyperplane further from the Moon offer exterior transfers. Hyperplane crossing maps similar to Figure 16 are generated for departure and arrival maneuver magnitude of 20 m/s and 40 m/s along the NRHO and the DRO, respectively. The maneuvers are delivered in the maximum stretching directions, type 'A' and type 'B'. Two different combinations of departure and arrival crossings on the map yield transfer geometries as observed in Figures 18(a) and 18(c). In contrast, an optimal exterior type geometry in Figure 18(b) is extracted from an initial guess on the map generated by maneuvers of magnitude 20 m/s to depart the NRHO and arrive on the DRO. Maps generated by other maneuver magnitudes may offer other transfer trajectory options. Figure 18(a) illustrates spacecraft motion near the Earth vicinity while Figures 18(b) and 18(c) include trajectories that leave further from the Earth-Moon vicinity. The maneuver costs, time of flight and the locations on the orbit for departure and arrival are listed in Table 2. Recall that the NRHO orbit and the DRO orbit possess different energy levels and, as a result, a ballistic transfer is not possible in the CR3BP. A theoretical minimum $|\Delta\bar{v}|$ is required to match the energy levels.

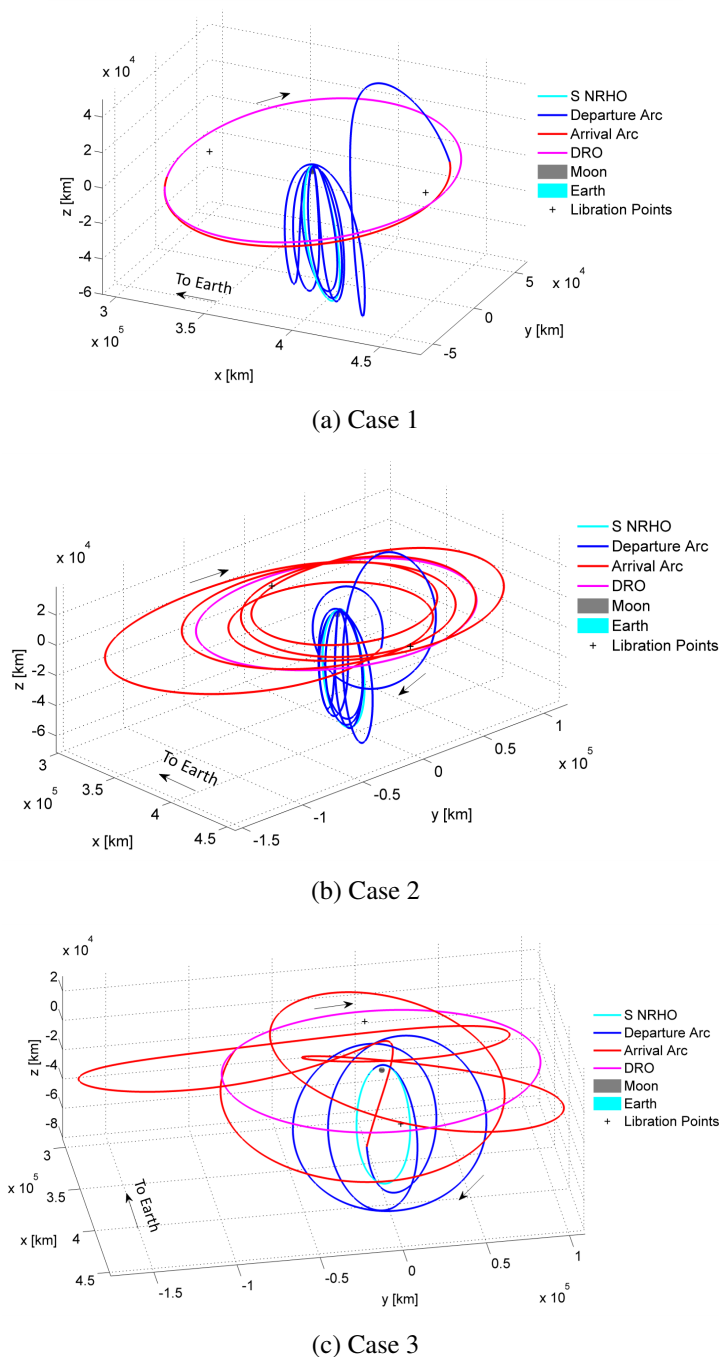


Figure 17: Interior type locally optimal transfer between L2 southern 9:2 synodic resonant NRHO to 70,000 km DRO.

Various transfer methodologies have been explored for transfers between the NRHO and the DRO in the literature, including low thrust trajectories, intermediate resonant structures and other known orbits.^{6–10,36} The examples in this investigation demonstrate the capability of leveraging maximum stretching directions for transfer trajectory design process to transition between a 3-dimensional NRHO to a planar DRO, without any prior knowledge of existing intermediate structures. Some of the transfer geometries, times of flight and maneuver costs are consistent with the literature.

CONCLUDING REMARKS

The current focus is on the Gateway mission, that potentially hosts humans on-board and is expected to remain in an almost stable 9:2 synodic resonant orbit in the southern L2 NRHO family. An approach suitable to transfer from the baseline NRHO to various locations relatively quickly while avoiding collisions with any vehicles is of relevance. The focus of this investigation is to leverage the maximum stretching direction as a tool to facilitate departure from the NRHO.

Stretching directions are a useful tool that assists in visualizing dynamical flow near a reference orbit. The maximum stretching directions, are leveraged for two contrasting applications. Station-keeping maneuvers as demonstrated by Muralidharan and Howell^{11,12,14} that are perpendicular to the maximum stretching directions minimize the magnitude of deviation from the reference orbit, while the orbit departure problem leverages maneuvers aligned in the maximum stretching direction to deliberately deviate from the reference orbit, and to eventually arrive on some destination orbit. Along a departure arc, propagated forwards in time, the maximum stretching direction offers the direction along which a maneuver delivers the maximum magnitude of state variation at final time. Similarly, the maximum stretching direction along a backward propagated arc, offers the region with maximum access to arrive on the orbit of interest with the smallest maneuver, in a linear sense. Such a tool is demonstrated for transfers between nearly stable orbits; a 3-dimensional southern

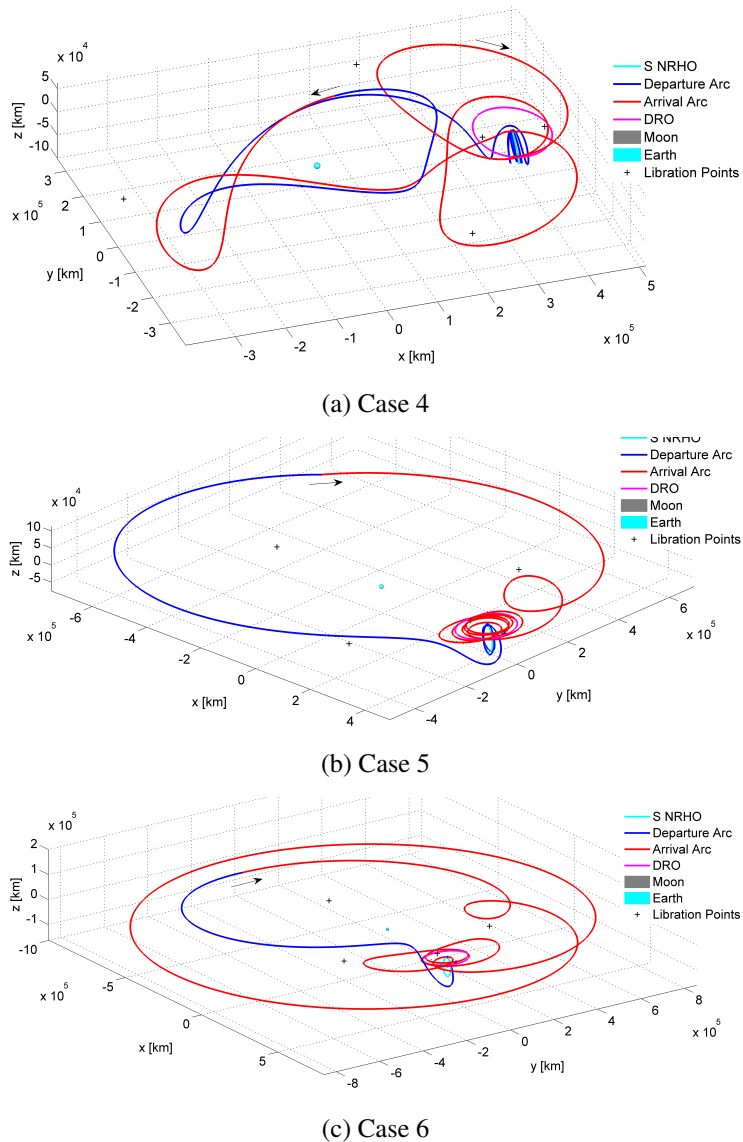


Figure 18: Exterior type locally optimal transfer between L2 southern 9:2 synodic resonant NRHO to 70,000 km DRO.

NRHO to a 3-dimensional northern NRHO, as well as a 3-dimensional NRHO to a planar DRO.

Table 2: Optimal transfers between 9:2 synodic resonant southern L2 NRHO to 70000 km DRO.

Parameter	Case 1	Case 2	Case 3	Case 4	Case 5	Case 6
	Figure 17(a)	Figure 17(b)	Figure 17(c)	Figure 18(a)	Figure 18(b)	Figure 18(c)
$ \Delta\bar{v}_{dep} $ [m/s]	4.03	3.81	15.06	12.41	4.41	18.62
$ \Delta\bar{v}_{int} $ [m/s]	355.51	306.24	172.71	81.38	120.30	296.08
$ \Delta\bar{v}_{arr} $ [m/s]	12.69	18.77	148.19	106.35	18.16	36.72
$ \Delta\bar{v}_{Total} $ [m/s]	372.23	328.81	335.97	200.14	142.88	351.41
ToF_{dep} [days]	44.42	50.29	28.28	63.15	54.36	36.51
ToF_{arr} [days]	6.96	64.49	49.69	78.81	111.52	130.65
ToF_{Total} [days]	51.39	114.79	77.97	141.96	165.88	167.15
TA_{dep} [deg]	37.75	7.85	255.08	129.27	339.64	354.57
κ [deg]	330.09	165.35	302.78	295.29	137.79	356.64

ACKNOWLEDGEMENTS

The authors are grateful to the members of the Multi-Body Dynamics Research Group for the insightful discussions. Facilities provided by the School of Aeronautics and Astronautics at Purdue University as well as the Rune and Barbara Eliassen Visualization Laboratory is appreciated. The first author acknowledges the support from the Purdue University Minority Engineering Program.

REFERENCES

- [1] E. M. Zimovan, K. C. Howell, and D. C. Davis, "Near rectilinear halo orbits and their application in cis-lunar space," *3rd IAA Conference on Dynamics and Control of Space Systems, Moscow, Russia*, 2017.
- [2] D. Guzzetti, E. M. Zimovan, K. C. Howell, and D. C. Davis, "Stationkeeping Analysis for Spacecraft in Lunar Near Rectilinear Halo Orbits," *27th AAS/AIAA Space Flight Mechanics Meeting, San Antonio, Texas, USA*, February 2017, pp. 1–20.
- [3] I. Cavallari, R. Petitdemange, and S. Lizy-Destrez, "Transfer from a Lunar distant retrograde orbit to mars through Lyapunov orbits," *27th International Symposium on Space Flight Dynamics (ISSFD), Melbourne, Australia*, Engineers Australia, Royal Aeronautical Society, 2019, pp. 1393–1398.
- [4] R. Martinez, K. E. Goodliff, and R. J. Whitley, "ISECG global exploration roadmap: A stepwise approach to deep space exploration," *AIAA SPACE 2013 Conference and Exposition, San Diego, California, United States*, 2013.
- [5] D. D. Mazanek, R. G. Merrill, J. R. Brophy, and R. P. Mueller, "Asteroid redirect mission concept: a bold approach for utilizing space resources," *Acta Astronautica*, Vol. 117, 2015, pp. 163–171.
- [6] B. J. P. Pino, K. C. Howell, and D. Folta, "An energy-informed adaptive algorithm for low-thrust spacecraft cislunar trajectory design," *AAS/AIAA Astrodynamics Specialist Conference, South Lake Tahoe, California, United States*, 2020.
- [7] S. Vutukuri, "Spacecraft Trajectory Design Techniques Using Resonant Orbits," M.S. Thesis, Purdue University, 2018.
- [8] A. Das-Stuart, K. C. Howell, and D. C. Folta, "Rapid trajectory design in complex environments enabled by reinforcement learning and graph search strategies," *Acta Astronautica*, Vol. 171, 2020, pp. 172–195.
- [9] E. M. Zimovan-Spreen and K. C. Howell, "Dynamical structures nearby NRHOS with applications in cislunar space," *AAS/AIAA Astrodynamics Specialist Conference, Portland, Maine, USA*, 2019.
- [10] L. R. Capdevila and K. C. Howell, "A transfer network linking Earth, Moon, and the triangular libration point regions in the Earth-Moon system," *Advances in Space Research*, Vol. 62, No. 7, 2018, pp. 1826–1852.
- [11] V. Muralidharan and K. C. Howell, "Stationkeeping in Earth-Moon Near Rectilinear Halo Orbits," *AAS/AIAA Astrodynamics Specialist Conference, South Lake Tahoe, California, USA*, August 2020.

- [12] V. Muralidharan and K. C. Howell, "Orbit Maintenance Strategy for Earth-Moon Halo Orbits," *31st AAS/AIAA Spaceflight Mechanics Meeting, Charlotte, North Carolina, USA (Virtual)*, February 2021.
- [13] V. Muralidharan, "Orbit Maintenance Strategies for Sun-Earth/Moon Libration Point Missions: Parameter Selection for Target Point and Cauchy-Green Tensor Approaches," M.S. Thesis, Purdue University, 2017.
- [14] V. Muralidharan, *Stretching Directions in Cislunar Space: Stationkeeping and an Application to Transfer Trajectory Design*. Ph.D. Dissertation, Purdue University, 2021.
- [15] K. Oshima, S. Campagnola, C. H. Yam, Y. Kayama, Y. Kawakatsu, N. Ozaki, Q. Verspieren, K. Kakihara, K. Oguri, and R. Funase, "EQUULEUS mission analysis: design of the transfer phase," *International Symposium on Space Technology and Science, ISTS-2017-d-159, Ehime, Japan, 2017*, pp. 3–9.
- [16] K. Oguri, K. Oshima, S. Campagnola, K. Kakihara, N. Ozaki, N. Baresi, Y. Kawakatsu, and R. Funase, "EQUULEUS Trajectory Design," *The Journal of the Astronautical Sciences*, Vol. 67, No. 3, 2020, pp. 950–976.
- [17] N. Baresi, D. A. Dei Tos, H. Ikeda, and Y. Kawakatsu, "Trajectory Design and Maintenance of the Martian Moons eXploration Mission Around Phobos," *Journal of Guidance, Control, and Dynamics*, Vol. 44, No. 5, 2021, pp. 996–1007.
- [18] C. Spreen, K. Howell, and B. Marchand, "Node placement capability for spacecraft trajectory targeting in an ephemeris model," *AAS/AIAA Astrodynamics Specialist Conference, Vail, Colorado, 2015*.
- [19] C. R. Short, D. Blazevski, K. C. Howell, and G. Haller, "Stretching in phase space and applications in general nonautonomous multi-body problems," *Celestial Mechanics and Dynamical Astronomy*, Vol. 122, No. 3, 2015, pp. 213–238.
- [20] V. Szebehely, "Theory of orbits: the restricted problem of three bodies," tech. rep., Yale univ New Haven CT, 1967.
- [21] K. C. Howell, "Three-dimensional, periodic, 'halo' orbits," *Celestial mechanics*, Vol. 32, No. 1, 1984, pp. 53–71.
- [22] G. Haller, "Lagrangian coherent structures from approximate velocity data," *Physics of fluids*, Vol. 14, No. 6, 2002, pp. 1851–1861.
- [23] C. R. Short and K. C. Howell, "Lagrangian coherent structures in various map representations for application to multi-body gravitational regimes," *Acta Astronautica*, Vol. 94, No. 2, 2014, pp. 592–607.
- [24] D. C. Davis, S. M. Phillips, K. C. Howell, S. Vutukuri, and B. P. McCarthy, "Stationkeeping and transfer trajectory design for spacecraft in cislunar space," *AAS/AIAA Astrodynamics Specialist Conference, Stevenson, Washington, USA, August 2017*.
- [25] K. K. Boudad, D. C. Davis, and K. C. Howell, "Disposal trajectories from near rectilinear halo orbits," *AAS/AIAA Astrodynamics Specialists Conference, Snowbird, Utah, USA, 2018*.
- [26] K. C. Howell and M. Kakoi, "Transfers between the Earth-Moon and Sun-Earth systems using manifolds and transit orbits," *Acta Astronautica*, Vol. 59, No. 1-5, 2006, pp. 367–380.
- [27] K. Howell, M. Beckman, C. Patterson, and D. Folta, "Representations of invariant manifolds for applications in three-body systems," *The Journal of the Astronautical Sciences*, Vol. 54, No. 1, 2006, pp. 69–93.
- [28] A. F. Haapala, "Trajectory design using periapse maps and invariant manifolds," M.S. Thesis, Purdue University, 2010.
- [29] J. Stuart, M. Ozimek, and K. Howell, "Optimal, low-thrust, path-constrained transfers between libration point orbits using invariant manifolds," *AIAA/AAS Astrodynamics Specialist Conference, Toronto, Canada, 2010*.
- [30] S. Soldini, C. Colombo, and S. J. Walker, "Solar radiation pressure end-of-life disposal for Libration-point orbits in the elliptic restricted three-body problem," *AAS/AIAA Space Flight Mechanics Meeting, Williamsburg, Virginia, USA, 2015*.
- [31] Z. Olikara, G. Gómez Muntané, and J. Masdemont Soler, "End-of-life disposal of libration point orbit spacecraft," *64rd International Astronautical Congress, Beijing, China, 2013*, pp. 1–13.
- [32] D. C. Davis, K. K. Boudad, S. M. Phillips, and K. C. Howell, "Disposal, deployment, and debris in near rectilinear halo orbits," *29th AAS/AIAA Space Flight Mechanics Meeting, Ka'anapali, Maui, Hawaii, USA, 2019*.
- [33] M. O. Ward, "A taxonomy of glyph placement strategies for multidimensional data visualization," *Information Visualization*, Vol. 1, No. 3-4, 2002, pp. 194–210.
- [34] A. F. Haapala and K. C. Howell, "Representations of higher-dimensional Poincaré maps with applications to spacecraft trajectory design," *Acta Astronautica*, Vol. 96, 2014, pp. 23–41.
- [35] B. J. P. Pino, *Energy-Informed Strategies For Low-Thrust Trajectory Design in Cislunar Space*. Ph.D. Dissertation, Purdue University, 2020.
- [36] R. E. Pritchett, *Strategies for Low-Thrust Transfer Design Based on Direct Collocation Techniques*. Ph.D. Dissertation, Purdue University, 2020.